Optimized permanent-magnet loops and arcs for improved field uniformity

Chris Morley,[1,*] Peter J. Hobson,[1] Noah Hardwicke,[1] Harriet O'Brien,[1] Niall Holmes,[1,2] and Mark Fromhold[1]

[1]*School of Physics & Astronomy, University of Nottingham, NG7 2RD, United Kingdom*
[2]*Sir Peter Mansfield Imaging Centre, University of Nottingham, NG7 2RD, United Kingdom*

(Received 30 June 2026; revised 23 September 2026; accepted 14 October 2026; published 16 November 2026)

Simple, low-cost, permanent magnet geometries are frequently used for field generation in cases where a constant high-strength magnetic field is required. This is the situation across many emerging quantum platforms, primarily for bias fields in quantum computing or nitrogen-vacancy centers. Finding optimal arrangements of primitive magnet geometries such as these can be difficult, often escalating in complexity, as further higher-order field harmonics are considered. This is further complicated by the need to adhere to strict system constraints, for instance, those implied by geometric or optical access requirements. Here we illustrate a method that encodes loop and arc magnet geometries into an analytical form, attaining solutions for the field harmonics produced by both axial and radial magnetizations for each form. These harmonic descriptions then form the basis of a numerical design procedure. Our approach facilitates solutions that improve fidelity of the target field by reducing error harmonic contributions while satisfying constraints on magnet position. This allows for considerations such as optical access or maximum system extents to be accounted for. To demonstrate this optimization procedure, we produce four system designs: two axially magnetized loops to produce a uniform axial field and two radially magnetized arcs, which, respectively, produce a radial-uniform and radial-gradient field. Their performance is then compared against standard designs, obtained from analytical solutions alone. In each case, when using our approach, the volume of field uniformity within 99% agreement of the target field increases by a minimum factor of 1.37. Designs generated by this procedure therefore enable improved field fidelity and reduce magnetic field-driven errors.

DOI: 10.1103/8nkv-46hc

I. INTRODUCTION

Magnetic field control is crucial in many experimental systems, particularly in the emerging fields of quantum technologies. Here it is used to control quantum systems, including state manipulation [1], atom trapping [2,3], and as quantization bias fields for systems such as optically pumped magnetometers (OPMs), cold atom inertial sensors, and atom interferometry [4–6]. However, when left improperly controlled or unshielded, magnetic fields also cause measurement errors, for example, phase shifts in quantum gravimeters [7,8] and cross-axis projection error in OPM sensors [9,10]. As a result, research into uniform magnetic field generation has been undertaken to address these issues in electromagnetic coil operation, including the target-field methods developed by Turner [11] and the work done to exploit magnetic field symmetries undertaken by Romeo and Hoult [12]. Recent work has built on both of these methods to optimize coil patterns in the presence of passive shielding [13–15] and develop a robust optimization procedure for discrete primitive coil shapes [16].

Permanent magnets are frequently used for many applications, particularly in cases where a constant high-strength magnetic field is required. Electromagnets tend to be unfavorable in such cases not only due to just power efficiency concerns but also thermal heating challenges, which may affect optical elements and require the additional bulk of water cooling apparatus to address. As a result, permanent magnets have found usage in Zeeman slowers [17,18], ion pumps [19], nuclear magnetic resonance and magnetic resonance imaging [20–22], nitrogen-vacancy (N-V) center magnetometry development [23], and as bias fields for quantum computing [24,25]. In each of these cases, the magnetic material can be tailored for its magnetization direction, shape, volume, strength, temperature stability, and resistance to external fields.

A crucial consideration in many of these applications is the uniformity of the field in the region of interest,

*Contact author: christopher.morley2@nottingham.ac.uk

Published by the American Physical Society under the terms of the Creative Commons Attribution 4.0 International license. Further distribution of this work must maintain attribution to the author(s) and the published article's title, journal citation, and DOI.

as deviations away from a defined field often cause errors or other complications. Inconsistencies in magnetic field across N-V center samples and arrays can lead to deviations in the returned signal, as different vacancy centers experience different fields [26]. Variations in the fields required for ion trap quantum computers can have detrimental effects on the lifetimes of qubits or lead to variation between what should be identical qubit sites [27,28]. One area of significant focus has been nuclear magnetic resonance, which has led to the development of methods to facilitate the design and optimization of passive shimming systems where small permanent magnets are applied around the bore to reduce field error [29–31]. The analysis and optimization of magnetized surfaces, meshes, and volumes are of interest across a variety of areas of physics from cold atoms to fusion [32–35]. Many of these methods tend to be computationally intensive, which can reduce resolution and offer limited insight into the physical nature of the system. This inspired our previous work to develop a permanent magnet focused target-field method [36].

While these methods provide exceptional field fidelity over the target region, they can be functionally impractical in some instances, requiring the placement of many small discrete magnetic pixels to build the complex magnetization pattern. They are also limited by discretization error, where the pixel mesh is not suitably fine, limiting the fidelity to which the magnetization can be replicated. Similarly, such methods may be infeasible for high-strength field requirements, where simpler geometries tend to be more viable to produce. In such cases, simple geometries, where the system parameters can be set to remove unwanted error variations (error harmonics)—in a similar manner to Helmholtz or anti-Helmholtz coils—can prove more effective. Such symmetry matching techniques for these simple building blocks (referred to as *primitives* henceforth) were suggested previously by Romeo and Hoult, specifically for loops and point pixels [12]. However, the design of systems that null higher-order variations, often containing multiple primitives, can be challenging, with each additional primitive requiring more harmonics to be considered, increasing complexity. Furthermore, previous implementations of this method focus solely on axially magnetized magnets, with radially magnetized systems (another standard manufacturing arrangement) neglected.

There have been many numerical approaches to tackle this problem for sets of primitive coils [37,38], but work on permanent magnets has focused on arrays of pixel magnets and topological optimization [39,40]. Similar methods have also been developed for Halbach arrays, arrangements of magnetized pixels that produce a self-shielding effect and have many uses across different sectors [41–43].

In this paper, we present a method for optimizing the spacing of nested primitive geometry and permanent magnetic arrays, reducing error contributions, and improving field uniformity. This is accomplished by encoding sets of primitives, in the form of loops and arcs, in two separate magnetization directions (axial $\hat{z}$ and radial $\hat{\rho}$) into a Green's function formulation of the magnetic scalar potential. This allows a direct comparison to the spherical harmonic magnitudes of the magnetic field decomposition. The analytical expressions governing the expansion coefficients in each case are calculated by solving the resulting integral expressions for each magnetization direction and geometry. To determine the best arrangements, we employ a similar optimization algorithm to that described in Ref. [16], where the separation of the various primitive elements is varied to remove error harmonics while maximizing the contribution from the target-field harmonic. Three examples of this process are considered: one zonal harmonic and two tesserals corresponding to axially magnetized loops and radially magnetized arcs, respectively. The resulting volume where the field deviates by less than 1% from the target field is then compared between the basic and fully optimized designs.

II. MATHEMATICAL MODEL

A. Spherical harmonic basis

We consider a region of space containing no electrical currents, and only permanent magnets with a fixed magnetization (neglecting hysteresis effects), $\mathbf{M}$, such that $\mathbf{B} = \mu_0(\mathbf{H} + \mathbf{M})$. Applying Ampere's law, $\nabla \times \mathbf{H} = 0$, and Gauss' law of magnetism, $\nabla \cdot \mathbf{H} = -\nabla \cdot \mathbf{M}$, gives the Poisson equation [44],

$$\nabla^2 \Psi(\mathbf{r}) = \nabla \cdot \mathbf{M}(\mathbf{r}), \tag{1}$$

where $\mathbf{M}(\mathbf{r})$ models the geometric spatial distribution of magnetic material (of constant strength and magnetization direction). Assuming that we are only interested in the scalar potential generated at a point $\mathbf{r}$ outside the material body of an arbitrary arrangement of permanent magnets, this simplifies to the Laplace equation,

$$\nabla^2 \Psi(\mathbf{r}) = 0. \tag{2}$$

Thus, as a solution set for the Laplace equation, a spherical harmonic basis can be used to decompose the current-free magnetic field produced. The magnetic scalar potential can thus be written,

$$\Psi(\mathbf{r}) = -\sum_{n=0}^{\infty} \sum_{m=-n}^{n} f_{n,m} R_{n,m}(\mathbf{r}), \tag{3}$$

where $f_{n,m}$ is the expansion coefficient associated with each harmonic and $R_{n,m}$ can be related to the real spherical harmonic of order n and degree m, respectively, i.e.,

$$R_{n,m}(r, \theta, \phi) = \eta_{n,m} r^n Y_{n,m}(\theta, \phi), \tag{4}$$

where $Y_{n,m}$ represents the real spherical harmonic,

$$Y_{n,m}(\theta,\phi) = P_{n,|m|}(\cos\theta)\begin{pmatrix}\cos(m\phi)\\ \sin(|m|\phi)\end{pmatrix}\quad\begin{matrix}m\geq 0\\ m<0\end{matrix}, \tag{5}$$

with $|m|\not> n$ due to Ferrer's associated Legendre polynomials, $P_{n,|m|}(\cos\theta)$. These describe the azimuthal dependence and are normalized such that

$$\eta_{n,m}\eta_{n',m'}\int_0^{\pi} d\theta \int_0^{2\pi} d\phi\, Y_{n,m}(\theta,\phi)Y_{n',m'}(\theta,\phi) = \delta_{n,n'}\delta_{m,m'}, \tag{6}$$

where

$$\eta_{n,m} = \sqrt{\frac{\zeta_{m,0}(2n+1)}{4\pi}\frac{(n-|m|)!}{(n+|m|)!}}. \tag{7}$$

Here, $\zeta_{m,m'} = 2-\delta_{m,m'}$, with $\delta_{m,m'}$ the Kronecker delta function.

The magnetic field is the gradient of the magnetic scalar potential,

$$\mathbf{B}(\mathbf{r}) = -\mu_0\nabla_{\mathbf{r}}\Psi(\mathbf{r}). \tag{8}$$

Substituting Eq. (8) into Eq. (3) allows the magnetic field to be expressed in terms of spherical harmonics,

$$\mathbf{B}(\mathbf{r}) = \mu_0\sum_{n=1}^{\infty}\sum_{m=-n}^{n} f_{n,m}\mathbf{B}_{n,m}(\mathbf{r}). \tag{9}$$

Here, $\mathbf{B}_{n,m}(\mathbf{r}) = \nabla_{\mathbf{r}}(R_{n,m}(\mathbf{r}))$ are the harmonics that manifest themselves in the magnetic field, and thus are referred to as the field harmonics. Examples of such harmonics have been long documented, including constant fields such as,

$$\mathbf{B}_{1,0} = \frac{1}{2}\sqrt{\frac{3}{\pi}}\hat{z}, \tag{10}$$

$$\mathbf{B}_{1,1} = \frac{1}{2}\sqrt{\frac{3}{\pi}}\hat{x}, \tag{11}$$

and linear gradient fields, including

$$\mathbf{B}_{2,0} = \frac{1}{2}\sqrt{\frac{5}{\pi}}(-x\hat{x}-y\hat{y}+2z\hat{z}), \tag{12}$$

$$\mathbf{B}_{2,1} = \frac{1}{2}\sqrt{\frac{15}{\pi}}(z\hat{x}+x\hat{z}). \tag{13}$$

Generalizing to larger n creates higher-order harmonics (we refer the reader to Appendix A of Ref. [16] for general equations). Typically, harmonics with degree $m=0$ are referred to as *zonal* harmonics, with other harmonics referred to as *tesseral* harmonics. Consequently, to optimize a set of arbitrary magnets to increase their uniformity, we can simply tailor the expansion coefficients in Eq. (3) to reduce contributions from unwanted field harmonics, $\mathbf{B}_{n,m}(\mathbf{r})$, while maximizing contributions from the target field. All that remains is to relate such a set of magnets to the spherical harmonics and determine expressions for each $f_{n,m}$ expansion coefficient.

B. Expansion coefficient formulation

Considering the scalar potential for ease of analysis, Eq. (2) may be solved for the scalar field at a point $\mathbf{r}$ from a set of magnets at position $\mathbf{r}'$ using the Green's functions formalism for the magnetic scalar potential,

$$\Psi(\mathbf{r}) = -\frac{1}{4\pi}\int d\mathbf{r}'\,\frac{\nabla_{\mathbf{r}'}\cdot\mathbf{M}(\mathbf{r}')}{|\mathbf{r}-\mathbf{r}'|}. \tag{14}$$

Enforcing that the magnetization is uniform within the permanent magnet, $\nabla_{\mathbf{r}'}\cdot\mathbf{M}(\mathbf{r}')=0$, we can then state,

$$\Psi(\mathbf{r}) = -\frac{1}{4\pi}\int d\mathbf{r}'\,\mathbf{M}(\mathbf{r}')\cdot\nabla_{\mathbf{r}'}\left(\frac{1}{|\mathbf{r}-\mathbf{r}'|}\right). \tag{15}$$

To match the symmetries, we then make use of the spherical harmonic representation of the Green's function,

$$\frac{1}{|\mathbf{r}-\mathbf{r}'|} = \sum_{n=0}^{\infty}\sum_{m=-n}^{n}\frac{(n-|m|)!}{(n+|m|)!}\frac{r^n}{(r')^{n+1}} \times Y_{n,m}(\theta,\phi)Y_{n,m}(\theta',\phi'), \tag{16}$$

where $Y_{n,m}(\theta',\phi')$ can be written following the same logic and is expressed according to Eq. (5).

We can simplify Eq. (15) by fixing the direction of the magnetization. In this paper, two cases will be considered, with the magnetization fixed in either the axial, $\mathbf{M}(\mathbf{r}') = M_z(\mathbf{r}')\hat{z}$, or radial, $\mathbf{M}(\mathbf{r}') = M_\rho(\mathbf{r}')\hat{\rho}$, direction of the cylindrical coordinate system. Substituting these, alongside Eq. (16) into Eq. (15), results in

$$\Psi_z(\mathbf{r}) = -\frac{1}{4\pi}\sum_{n=0}^{\infty}\sum_{m=-n}^{n} r^n Y_{n,m}(\theta,\phi)\int d\mathbf{r}'\,M_z(\mathbf{r}') \times\frac{\partial}{\partial z'}\left(\frac{(n-|m|)!}{(n+|m|)!}\frac{1}{(r')^{n+1}}Y_{n,m}(\theta',\phi')\right) \tag{17}$$

for the axially magnetized case and

$$\Psi_\rho(\mathbf{r}) = -\frac{1}{4\pi}\sum_{n=0}^{\infty}\sum_{m=-n}^{n} r^n Y_{n,m}(\theta,\phi)\int \mathrm{d}\mathbf{r}'\, M_\rho(\mathbf{r}') \times \frac{\partial}{\partial\rho'}\left(\frac{(n-|m|)!}{(n+|m|)!}\frac{1}{(r')^{n+1}}Y_{n,m}(\theta',\phi')\right) \quad (18)$$

for the radial case.

Differentiating and comparing these equations with Eq. (3) provides expressions for $f_{n,m}$ in each case. Namely,

$$f^z_{n,m} = -\frac{1}{4\pi\eta_{n,m}}\frac{(n-|m|+1)!}{(n+|m|)!} \times \int \mathrm{d}\mathbf{r}'\, M_z(\mathbf{r}')\frac{Y_{n+1,m}(\theta',\phi')}{(r')^{n+2}} \quad (19)$$

for axial magnetization and

$$f^\rho_{n,m} = \frac{1}{4\pi\eta_{n,m}}\frac{(n-|m|)!}{(n+|m|)!}\int \frac{\mathrm{d}\mathbf{r}'\, M_\rho(\mathbf{r}')}{\sin\theta'(r')^{n+2}} \times ((n-|m|+1)\cos\theta' Y_{n+1,m}(\theta',\phi') - (n+1)Y_{n,m}(\theta',\phi')) \quad (20)$$

for the radial. With these expressions, we can now input geometric descriptions of simple magnetic structures for $M_z(\mathbf{r}')$ and $M_\rho(\mathbf{r}')$ and determine the forms of $f_{n,m}$ for each magnetization direction. These can then be used to remove the magnitudes of error harmonics and improve the resulting field uniformity.

III. PRIMITIVE DESIGN

A. Magnetic loops

The first of the two structures to be analyzed comprises uniformly magnetized filamentary loops, each with radius ρ_c, positioned at $z = \pm d_c$ along the axial ($\hat{z}$) axis. The distribution of the magnetic material in such a system can be described by,

$$M_{\text{loops}}(\mathbf{r}') = M_0\delta(\rho'-\rho_c) \times [\delta(z'-d_c) \pm \delta(z'+d_c)], \quad (21)$$

where M_0 is the remanent magnetization of the magnets and the Dirac delta functions are $\delta(x-x_0)$. The $\pm$ of Eq. (21) denotes whether the magnetization direction is symmetric or antisymmetric across the axial axis. This geometry is illustrated for the antisymmetric case in Fig. 1. Equation (21) can then be substituted into both Eqs. (19) and (20), and the integral is evaluated to determine analytical expressions for the harmonic magnitudes in each case.

Focusing on the axially magnetized case initially and converting to cylindrical coordinates to evaluate the integral, $r^2 = (\rho^2+z^2)$ and $\cos\theta = z/\sqrt{\rho^2+z^2}$, provides

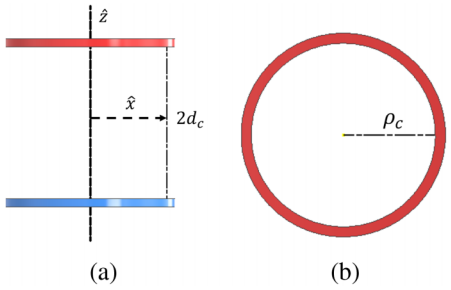


FIG. 1. Schematic illustration of antisymmetric loop pairs of radius ρ_c separated by $2d_c$ symmetrically around the z axis shown in (a) the xz plane and (b) the xy plane. Magnetization, M, orientated aligned with $\hat{\rho}$ or $\hat{z}$ is shown in red, while M orientated antialigned is shown in blue.

$$f^z_{n,0} = -\frac{(1\pm(-1)^{n+1})(n+1)M_0}{2\eta_{n,0}} \times \frac{\rho_c}{(\sqrt{\rho_c^2+d_c^2})^{(n+2)}}P_{n+1,0}\left(\frac{d_c}{\sqrt{\rho_c^2+d_c^2}}\right) = -\frac{(1\pm(-1)^{n+1})(n+1)M_{0z}}{2\eta_{n,0}\rho_c^{n+1}} \times \frac{1}{(\sqrt{1+\chi_c^2})^{(n+2)}}P_{n+1,0}\left(\frac{\chi_c}{\sqrt{1+\chi_c^2}}\right), \quad (22)$$

where $\chi_c = d_c/\rho_c$ is the normalized loop separation. This is used throughout to ease calculations, with ρ_c fixed for each design illustrated in Sec. IV. As expected, the symmetric magnet pair, (+), exclusively generates field harmonics of odd orders, and the antisymmetric magnetic pair, (−), exclusively generates field harmonics of even orders. It is also worth noting that loops can only generate *zonal* harmonics, as illustrated by Romeo and Hoult previously [12]. A similar process can be followed for the radially magnetized case, resulting in

$$f^\rho_{n,0} = \frac{(1\pm(-1)^n)M_0}{2\eta_{n,0}}\frac{\rho_c}{\left(\sqrt{\rho_c^2+d_c^2}\right)^{(n+2)}} \times P_{n+1,1}\left(\frac{d_c}{\sqrt{\rho_c^2+d_c^2}}\right) = \frac{(1\pm(-1)^n)M_0}{2\eta_{n,0}\rho_c^{n+1}}\frac{1}{\left(\sqrt{1+\chi_c^2}\right)^{(n+2)}} \times P_{n+1,1}\left(\frac{\chi_c}{\sqrt{1+\chi_c^2}}\right). \quad (23)$$

While the radially magnetized loops can comparably only generate $m = 0$ *zonal* harmonics, it should be noted that the relation between even and odd orders differs from that of Eq. (22). Here, the symmetric magnet pair (+) generates even orders, while the antisymmetric case (−)

generates odd orders, opposite to the axially magnetized case described in Eq. (22).

Optimizing a single pair of magnets in these configurations is relatively simple; one simply needs to minimize the contribution from the first-order error harmonic. To optimize a symmetric, axially magnetized, *Helmholtz* magnet loop pair to generate $\mathbf{B}_{1,0}$, we need to find a normalized loop separation, which sets $f_{3,0} = 0$, thereby eliminating the contribution from $\mathbf{B}_{3,0}$ as the leading-order error harmonic. For the axially magnetized case, this requires $P_{4,0}(x) = (1/8)(35x^4 - 30x^2 + 3) = 0$, which has roots at $x = \pm\sqrt{(15 \pm 2\sqrt{30})/35}$. Thus, the required normalized separations are

$$\chi_c = \frac{1}{2}\sqrt{6 \pm \sqrt{30}} = [0.3615, 1.6939]. \tag{24}$$

In contrast to previous work [16], there are two roots, which remove the contributions from $f_{3,0}$ in this case. The smaller of these roots, $\chi_c = 0.3615$, produces a field aligned with negative z, while the larger, $\chi_c = 1.6939$, produces a field aligned with positive z. This occurs despite both arrangements being magnetized along the z axis. As noted, these results differ greatly from those expected for Helmholtz coils ($\chi_c = 0.5$ in this coordinate system), illustrating the fundamental harmonic differences between loops of axially magnetized magnetic material and loops of current-carrying wire; further details are provided in Appendix A. The resulting magnet arrangements and the corresponding $\mathbf{B}_{1,0}$ fields produced are shown in Fig. 2. Similar procedures can be followed in all the single pair loop cases for any harmonic and magnetization direction.

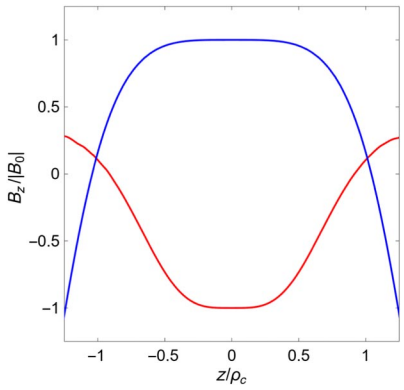


FIG. 2. The magnetic field generated from a pair of loops magnetized in the $\hat{z}$ direction with radius ρ_c and normalized separations $\chi_c = 0.3615$, shown in red, and $\chi_c = 1.6939$, shown in blue. The fields are normalized as $B_z/|B_0|$, where $B_0 = B_z(z = 0, \rho = 0)$.

B. Magnetic arcs

The second structure we will analyze is a set of uniformly magnetized arcs of radius ρ_c at axial positions $z = \pm d_c$. The arcs have opposing magnetization directions in the xy plane and, as above, can be constructed such that they are axially symmetric (+) or antisymmetric (−). Thus, the magnetic distribution of the arcs can be described as,

$$M_{\text{arcs}} = M_0\delta(\rho' - \rho_c)[\delta(z' - d_c) \pm \delta(z' + d_c)] \times \sum_{\lambda=0}^{1}(-1)^{\lambda}[H(\phi' + \phi_c - \lambda\pi) - H(\phi' - \phi_c - \lambda\pi)], \tag{25}$$

where $H(x)$ is the Heaviside step function and ϕ_c is the maximum angular extent of the arcs. The symmetric case is shown schematically in Fig. 3.

A similar method, as in Sec. III A, is then followed to determine the harmonic magnitudes in the axial and radial magnetization directions. For the axial direction, we determine the magnitudes to be given by,

$$f^z_{n,m} = -\frac{(1 \pm (-1)^{n+m+1})(n - m + 1)!M_{0z}}{\pi m(n + m)!\eta_{n,m}\rho_c^{n+1}} \times \frac{1}{(\sqrt{1 + \chi_c^2})^{(n+2)}} P_{n+1,m}\left(\frac{\chi_c}{\sqrt{1 + \chi_c^2}}\right)\sin(m\phi_c), \tag{26}$$

where $m \in (2\tilde{m} + 1)$ for $\tilde{m} \in \mathbb{Z}^{0+}$. Otherwise, $f^z_{n,m} = 0$. As expected, axially symmetric and antisymmetric sets of arcs only generate field harmonics dictated by whether the parity of $(n + m)$ is odd or even, respectively. This also suggests that such arcs are capable of making purely *tesseral* harmonics, an enhancement of the regime provided by Romeo and Hoult where generating such harmonics also produced zonal fields [12].

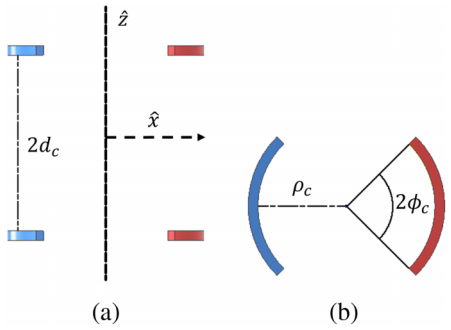


FIG. 3. Schematic illustration of arc pairs of radius ρ_c and angular separation $2\phi_c$, separated by $2d_c$ in the z axis shown in (a) the xz plane and (b) the xy plane. Magnetization, M, orientated aligned with $\hat{\rho}$ or $\hat{z}$ is shown in red, while M orientated antialigned is shown in blue.

Conversely, in the radially magnetized case, we determine,

$$f^{\rho}_{n,m} = \frac{(1\pm(-1)^{n+m})(n-m)!M_{0\rho}}{\pi m(n+m)!\eta_{n,m}\rho_c^{n+1}} \frac{1}{(\sqrt{1+\chi_c^2})^{(n+1)}} \times \left((n-m+1)\frac{\chi_c}{\sqrt{1+\chi_c^2}}P_{n+1,m}\left(\frac{\chi_c}{\sqrt{1+\chi_c^2}}\right) - (n+1)P_{n,m}\left(\frac{\chi_c}{\sqrt{1+\chi_c^2}}\right)\right)\sin(m\phi_c). \quad (27)$$

As before, $m \in (2\tilde{m}+1)$ for $\tilde{m} \in \mathbb{Z}^{0+}$. Otherwise, $f^{\rho}_{n,m} = 0$. The harmonics for axially symmetric or antisymmetric radially magnetized arcs also follow the same parity with respect to $(n+m)$ as the axially magnetized arcs. Unlike the previous examples, however, optimizing radially magnetized arcs requires one to find the roots of the sum of two associated Legendre polynomials, $P_{n+1,m}(x)$ and $P_{n,m}(x)$ to successfully null a target harmonic.

However, in contrast to loops, to optimize a simple single pair of arcs, an additional step is required. Namely, ϕ_c, the ideal arc length must be determined. This procedure follows the same approach as in Ref. [16], whereupon we note that all possible harmonics in Eqs. (26) and (27) depend upon $\sin(m\phi_c)$. Thus, we can substitute this into the relevant polynomial and find the roots of the function that null leading-order harmonics. With this in mind, generating a uniform transverse field, $\mathbf{B}_{1,1}$, using an axially antisymmetric set, requires nulling the field harmonics of degree $m = 3$. This is achieved by setting $\phi_c = \pi/3$. The separation can then be set to remove the contribution of the $n = 3$ harmonic, namely, $f_{3,1}$. For the axially magnetized case, this requires

$$\chi_c = \frac{\sqrt{3}}{2} = 0.8660, \quad (28)$$

which is determined by finding where the polynomial $P_{4,1}(x) = -(5x/2)(7x^2-3)\sqrt{1-x^2} = 0$, namely, at $x = [0, \pm\sqrt{3/7}, \pm 1]$.

These solutions, for both axially and radially orientated magnetization, can also be generalized to account for arc sets with $\tilde{M}$ fold azimuthal symmetry to null higher-order azimuthal harmonics. In either magnetization case, this magnetization distribution can be described by,

$$M_{\text{arcs}} = M_0\delta(\rho'-\rho_c)[\delta(z'-d_c)\pm\delta(z'+d_c)] \times \sum_{\lambda=0}^{2\tilde{M}-1}(-1)^{\lambda}\left[H\left(\phi'+\phi_c-\frac{\lambda\pi}{\tilde{M}}\right) - H\left(\phi'-\phi_c-\frac{\lambda\pi}{\tilde{M}}\right)\right], \quad (29)$$

resulting in

$$f^{z}_{n,m} = -\frac{(1\pm(-1)^{n+m+1})(n-m+1)!M_{0z}\tilde{M}}{\pi m(n+m)!\eta_{n,m}\rho_c^{n+1}} \frac{1}{(\sqrt{1+\chi_c^2})^{(n+2)}}P_{n+1,m}\left(\frac{\chi_c}{\sqrt{1+\chi_c^2}}\right)\sin(m\phi_c). \quad (30)$$

For the radially magnetized case, this similarly becomes

$$f^{\rho}_{n,m} = \frac{(1\pm(-1)^{n+m})(n-m)!M_{0\rho}\tilde{M}}{\pi m(n+m)!\eta_{n,m}\rho_c^{n+1}} \frac{1}{(\sqrt{1+\chi_c^2})^{(n+1)}}\left((n-m+1)\frac{\chi_c}{\sqrt{1+\chi_c^2}}P_{n+1,m} \times\left(\frac{\chi_c}{\sqrt{1+\chi_c^2}}\right) - (n+1)P_{n,m}\left(\frac{\chi_c}{\sqrt{1+\chi_c^2}}\right)\right)\sin(m\phi_c), \quad (31)$$

where, again, $m \in \tilde{M}(2\tilde{m}+1)$ for $\tilde{m} \in \mathbb{Z}^{0+}$.

It should be noted that both axial and radial magnetization directions can produce either zonal or tesseral harmonics, depending entirely on the primitive geometry choice. However, due to the difference in the analytical equations governing $f^{\rho}_{n,m}$ and $f^{z}_{n,m}$, the normalized separation required to null a given error harmonic can vary. As stated above, producing a $\mathbf{B}_{1,1}$ field requires the arc geometry and, for the axial case, a normalized separation of $\chi_c = 0.8660$. In contrast, for the radially magnetized arcs case, there are two solutions, $\chi_c = [0.3893, 2.5687]$ (this case is discussed in more detail in Sec. IV A). Both magnetizations are capable of producing the same field, but with different optimal geometries, giving additional flexibility when trying to incorporate the magnets into a constrained system. In an example system, an axially magnetized geometry may struggle to find an applicable optimum; a radial geometry may succeed and vice versa.

C. Nulling multiple error harmonics

Optimizing the sets of arc and loop primitives to null multiple error harmonics is more complex. Removing error harmonics higher than first order can be accomplished through the use of multiple magnets, with n additional magnets required to null up to the nth-order error harmonic. Similarly, generating a harmonic of nth order requires $n-1$ magnets. Thus, arguably, one can simply solve the solutions analytically for each harmonic targeted for removal and so improve field uniformity. However, in practice, this is difficult, as constraints on system size and other factors, such as experimental access make, this approach impractical, increasingly so when attempting to generate higher-order harmonics.

As a result, an optimization method is best employed. This allows us to exploit the rapid solutions provided through the established analytical framework while also creating a flexible algorithm for ease of integration into numerous systems. In this case, an optimization method similar to that established in Ref. [16] is used, which involves moving to an *underdetermined* problem, where we null fewer harmonics than there are magnet parameters. Determining an acceptable numerical solution in this situation becomes easier, and further constraints (such as maximum separation limits) can be more readily built into the algorithm, making it more flexible for practical use. Solutions can then prove easier to obtain at the expense of targeting fewer harmonics for nulling, thereby trading ultimate field uniformity for adaptability.

Optimization flexibility can also be improved by introducing a magnetization volume ratio, V, that governs the relative volume and therefore relative contribution of each set of magnets. This could be similarly accomplished by varying M_0, the remanent magnetization, of each set; however, the volume was chosen here to provide a standard integer ratio adjustment. This is similar to *winding ratios* in previous implementations, except rather than denoting, for example, a factor of I more windings on one electromagnet, they denote additional magnetic material. For example, $V_i = [1, -2]$ would suggest twice as much material on the second magnet, whose magnetization direction is orientated opposite to the first. The total coefficient for each $\mathbf{B}_{n,m}$ harmonic mode for the magnet system can then be ascertained from the summation over contributions for the N magnets,

$$F_{n,m} = \sum_{i=1}^{N} V_i f_{n,m}(\chi_{ci}), \tag{32}$$

where V_i is the volume ratio and χ_{ci} the normalized separation for the ith magnet. To null error harmonics up to order $n_{\max}$, for the target harmonic $F_{n,m}$, we can determine the total contribution to each error harmonic for the magnet set from Eq. (32). For each error harmonic that we wish to null, preceding $n_{\max}$, we seed the parameter space via a set of mesh points to feed into the FindRoot *Mathematica* function. These search the local area of the mesh point to determine a contour in the parameter space where the total contribution to each error harmonic, $F_{n,m}$, are zero; an example is shown in Fig. 4. This contour is then interpolated and used as a finer mesh to seed FindRoot again. This final set of solutions along this contour is then ranked by a desired property. The initial number of mesh points can be varied to provide a more detailed initial search. When a set of solutions is found on the contour in the optimization space, these are then ranked by a desired property. In this case, we chose the ratio of the desired harmonic magnitude to leading-order error harmonic magnitude. Thus, if we attempt to generate the harmonic $F_{n,m}$, nulled to the order of error $n_{\max}$, then we would aim to maximize $F_{n,m}/F_{n_{\max},m}$. As an example, to generate $\mathbf{B}_{1,0}$ while nulling up to the third-order error harmonic would involve finding the contour where $F_{3,0} = F_{5,0} = 0$ and then maximizing $F_{1,0}/F_{7,0}$. In this manner, the algorithm is able to minimize error while maximizing the contribution from the target harmonic.

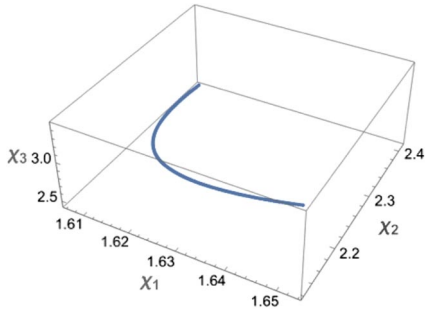


FIG. 4. A contour (blue) showing where two error harmonics equal zero for a three-magnet system, with $\chi_{\min} = 0.1$ and $\chi_{\max} = 3.5$. Note that each χ_i axis is limited for clarity.

We implement this solution in *Mathematica*, allowing the user to apply limits on $\chi_{\max}$ and $\chi_{\min}$, while inputting parameters such as relative volume ratios between each magnet. Practically, the relative volume ratios between magnets can be altered for each run of the optimization. The algorithm produces results in under a minute on a standard specification desktop (quad-core CPU, 8 GB DDR3 RAM), meaning that user input of the volume parameters proved more than suitable. Particularly when compared with the challenges of implementing an integer optimization to determine the volume parameters in conjunction with the existing algorithm.

IV. RESULTS

We now utilize the algorithm described in Sec. III to generate various commonly used magnetic field harmonics. In Sec. IV A, we detail how this can be used to generate uniform magnetic fields, $\mathbf{B}_{1,0}$ and $\mathbf{B}_{1,1}$, and compare the results to those generated by both a standard geometry (such as the χ_c values, determined analytically in Secs. III A and III B) and higher-order error harmonic nulling *nested* geometries. Gradient fields are then discussed in Sec. IV C, namely, the tesseral harmonic $\mathbf{B}_{2,1}$. For brevity, we limit the scope of the loop primitives to only axial magnetization and the arc primitives to only radial magnetization. As mentioned in Sec. III, both magnetization directions are compatible with either primitive geometry. All normalized magnet separations, χ_c, are determined by the optimization procedure described in Sec. III C, with the volume ratios, V_i, defined by user input. The resulting systems are then modeled in COMSOL, a multiphysics finite element method program, which is utilized to provide an independent determination

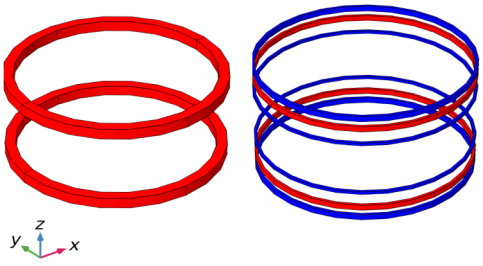
of the magnetic field. This analysis involved using the default equations, boundary conditions, and solvers found in the Magnetic Fields No Currents (mfnc) interface within the ac/dc module. All geometries were meshed finely enough such that the solution could be considered stable, which varied per arrangement modeled but typically required finer meshes on the more complex nested arrangements.

A. Uniform magnetic field generation: Loops

First, we look at optimizing a set of axially magnetized loop magnets to generate the target harmonic $\mathbf{B}_{1,0}$, described in Eq. (10). As discussed in Sec. III A, a simple single pair of loops has two solutions for this harmonic that remove the contribution of $\mathbf{B}_{3,0}$. These occur when magnets are placed at one of two normalized separations, $\chi_c = 0.3615$ or $\chi_c =, 1.6939$. To further improve the uniformity of these designs, harmonics $\mathbf{B}_{5,0}$ and $\mathbf{B}_{7,0}$ can also be nulled. A nested design of similar dimensions to $\chi_c = 0.3615$ was determined for comparison, with the magnetic field of each of these designs compared with determine the increase in uniformity.

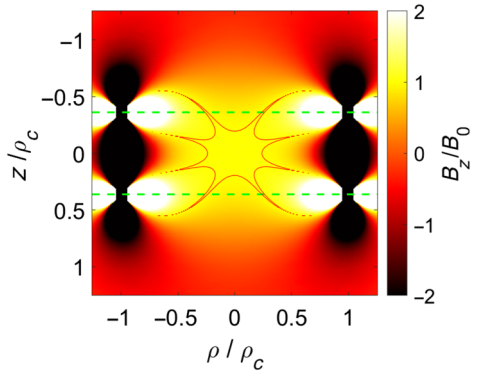
For the nested version of the $\chi_c = 0.3615$ design, the optimization was performed with $\chi_{\min} = 0.01$ and $\chi_{\max} = 0.5$. The volume ratios that were determined to give the best result by user input were $V_i = [-1, 2, -2]$, with the optimization procedure returning $\chi_c = [0.2481, 0.3995, 0.4999]$. Where the first χ_c value corresponds to the first V_i value and so on for all other values. This arrangement is illustrated in Fig. 5 along with the simple $\chi_c = 0.3615$ solution.

The magnetic field for both the single pair and nested set designs was simulated and compared in Fig. 6. Taking a target region between $\rho = -\rho_c$ to ρ_c and $z = -\rho_c$ to ρ_c, determining the magnetic field at a suitable number of points within this volume and comparing each point's percentage agreement to the target field, $\mathbf{B}_{1,0}$, it was determined that the volume of uniformity (defined where the field deviates from the target harmonic by



(a) (b)

FIG. 5. Schematic illustration of (a) a simple loop pair with $\chi_c = 0.3615$ and (b) a nested loop set with $\chi_c = [0.2481, 0.3995, 0.4999]$ and volume ratios of $V_i = [-1, 2, -2]$, in each case loops are of radius ρ_c and designed to generate $\mathbf{B}_{1,0}$. Magnetization orientated along positive (negative) $\hat{z}$ is shown in red (blue). The axis is common across both diagrams.



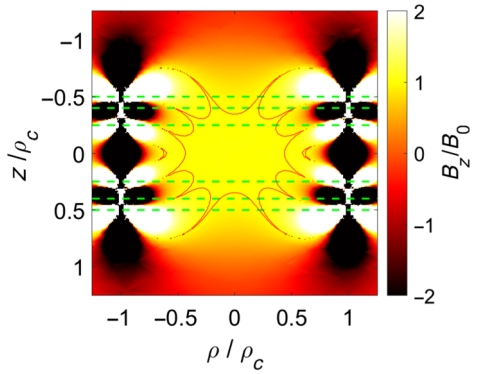


FIG. 6. Normalized axial ($\hat{\mathbf{z}}$) field, $\bar{B} = B_z/B_0$ (where $B_0 = B_z(z = 0, \rho = 0)$), plotted in the xz plane for (a) single loop magnet set with $\chi_c = 0.3615$ is shown in Fig. 5(a) and (b) nested loop set with $\chi_c = [0.2481, 0.3995, 0.4999]$ and volume ratios $V_i = [-1, 2, -2]$ is shown in Fig. 5(b). All magnets are magnetized in the $\hat{z}$ direction, ρ_c is kept constant across all figures, and all configurations are optimized to generate the $\boldsymbol{B}_{1,0}$ harmonic. Solid red contours enclose the area where the uniform B_z field deviates from uniformity by 1%, green dashed lines indicate positions of magnets in the xz plane.

greater than 1%) increases by a factor of 2.5635 from Figs. 6(a) and 6(b).

A nested version of similar dimensions to the simple $\chi_c = 1.6939$ case is detailed in Appendix B for clarity.

B. Uniform magnetic field generation: Arcs

In Sec. III, how to create $\mathbf{B}_{1,1}$ from an axially magnetized arc set that removes the $\mathbf{B}_{3,1}$ harmonic was discussed. For completeness, this section will focus on how to generate a highly uniform $\mathbf{B}_{1,1}$ from a radially magnetized set of arcs. Consulting Eq. (27), it can be seen that to set $f_{3,1} = 0$ requires finding the root of the polynomial $3xP_{4,1}(x) - 4P_{3,1}(x)$, where $x = \chi_c/\sqrt{1+\chi_c^2}$. This has two roots, with the normalized seperations required to remove the $\mathbf{B}_{3,1}$ harmonic being $\chi_c = [0.3893, 2.5687]$, with a corresponding $\phi_c = \pi/3$, which removes the $m = 3$ degree contribution.

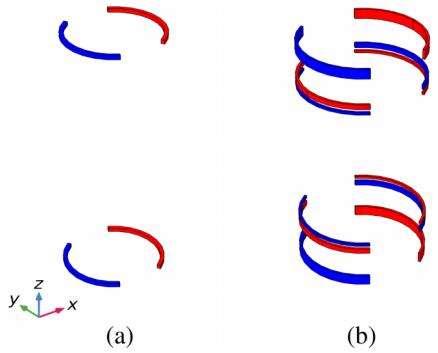


FIG. 7. Schematic illustration of (a) a simple arc pair set with $\chi_c = 2.5687$ and (b) a nested arc set with $\chi_c = [1.1758, 1.2879, 1.8399]$ and volume ratios of $V_i = [1, -2, 4]$. All arcs have radius ρ_c and are designed to generate $\mathbf{B}_{1,1}$. Magnetization orientated along positive (negative) $\hat{\rho}$ is shown in red (blue). The axis is common across both diagrams.

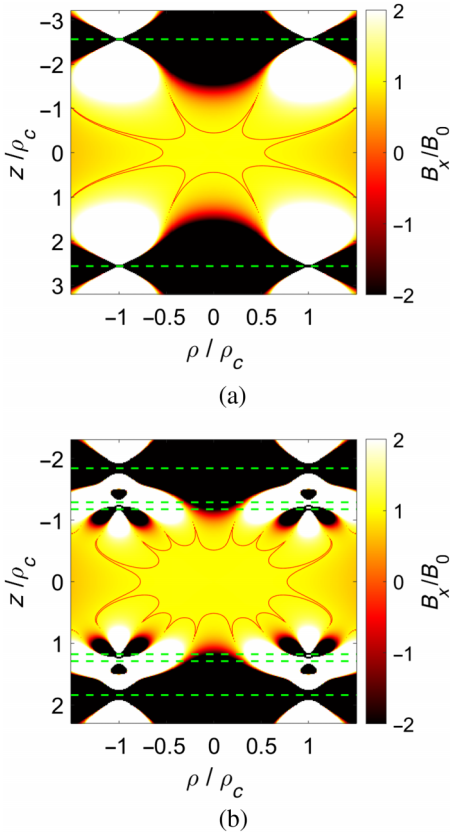


FIG. 8. Normalized $\hat{\mathbf{x}}$ field, $\bar{B} = B_x/B_0$ (where $B_0 = B_x(z = 0, \rho = 0)$), plotted in the xz plane for (a) single loop magnet set with $\chi_c = 2.5687$, shown in Figs. 7(a) and 7(b) nested loop set with $\chi_c = [1.1758, 1.2879, 1.8399]$ and volume ratios $V_i = [1, -2, 4]$ is shown in Fig. 7(b). All magnets are magnetized in the $\hat{\rho}$ direction, ρ_c is kept constant across all figures, and all configurations are optimized to generate the $\boldsymbol{B}_{1,1}$ harmonic. Solid red curves enclose the area where the uniform B_x fields deviate from uniformity by 1%, green dashed lines indicate positions of magnets in the xz plane.

As with the axial loop designs provided in this section, we compare the simple solution (specifically $\chi_c = 2.5687$) to a higher-order nested solution. Setting $\chi_{\min} = 0.7$ and $\chi_{\max} = 2.6$, it was determined, for a volume ratio set $V_i = [1, -2, 4]$, that the optimized normalized separations obtained are $\chi_c = [1.1758, 1.2879, 1.8399]$. Such a set of radially magnetized arcs would null up to order $\mathbf{B}_{7,1}$. In each case, ϕ_c was set to $\pi/3$ as before. A diagram illustrating this magnet arrangement is shown in Fig. 7. The single pair solution and the nested solution are contrasted in Fig. 8, which further illustrates the increase in uniformity provided by our method, with the uniform volume increasing by a factor of 1.37.

C. Gradient magnetic field generation

The optimization procedure is also capable of producing higher-order harmonics, such as linear gradients. To illustrate this, two solutions were obtained to generate the $\mathbf{B}_{2,1}$ harmonic, given by Eq. (13). In both cases, the required arc structures were magnetized radially as before, though solutions could equally be obtained for the axially magnetized case. The low-order solution, which removes the contribution of the $\mathbf{B}_{4,1}$ harmonic, is obtained via a radially antisymmetric magnetic arrangement with $\chi_c = 3.1290$ and $\phi_c = \pi/3$. The nested arrangement, designed to set $f_{4,1} = f_{6,1} = 0$ and minimize contributions from $f_{8,1}$, has $\chi_c = [1.5381, 1.6335, 2.0888]$ and volume ratios of $V_i = [1, -2, 3]$. This was attained from limits on χ_c of $\chi_{\min} = 1$ and $\chi_{\max} = 3$. This arrangement is illustrated in Fig. 9.

The magnetic field from each arrangement and divergence from the required harmonic are compared in Fig. 10. The nested magnet arrangement illustrated in Fig. 9(b)

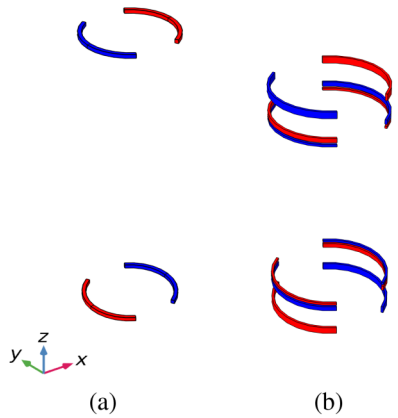


FIG. 9. Schematic illustration of (a) a simple arc set with $\chi_c = 3.1290$ and (b) a nested arc set with $\chi_c = [1.5381, 1.6335, 2.0888]$ and volume ratios of $V_i = [1, -2, 3]$, respectively. All arcs are of radius ρ_c and designed to generate $\mathbf{B}_{2,1}$. Magnetization along positive (negative) $\hat{\rho}$ is shown in red (blue). The axis is common across both diagrams.

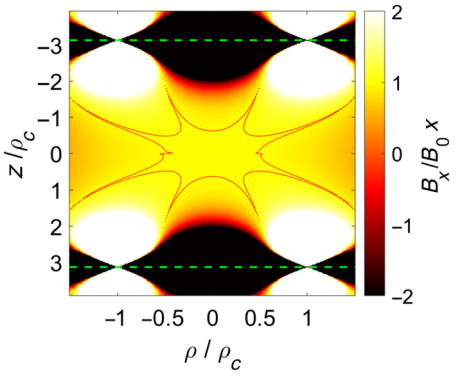


FIG. 10. Normalized $\hat{x}$ field, $\bar{B} = B_x/B_0 x$ (where B_0 is obtained from a fit around the origin), plotted in the xz plane for (a) single loop magnet set with $\chi_c = 3.1290$ is shown in Fig. 9(a) and (b) nested loop magnet set with $\chi_c = [1.5381, 1.6335, 2.0888]$ and magnetization ratios $M_i = [1, -2, 3]$ is shown in Fig. 9(b). All magnets are magnetized in the $\hat{\rho}$ direction, ρ_c is kept constant across all figures, and both configurations are optimized to generate the $\boldsymbol{B}_{2,1}$ harmonic. Solid red contours enclose the area where the uniform B_x fields deviate from uniformity by 1%, green dashed lines indicate positions of magnets in the xz plane.

increases the region of uniformity by a factor of 1.59 compared with the simple geometry of Fig. 9(a).

Similar methods could be utilized to obtain an optimized zonal harmonic, such as $\mathbf{B}_{2,0}$. This requires following the same optimization procedures but for antisymmetric loop structures. As before, these can be magnetized axially or radially, giving additional geometric options that may fit with different geometric requirements.

V. DISCUSSION

As seen in Sec. IV, the optimization procedure produces increased field fidelity across both geometries and magnetization directions. The flexibility of the optimization, alongside the use of constraints on χ_c and volume ratios, facilitates implementation into a variety of experimental constraints, such as those imposed by optical access requirements. This is further advanced by the choice of two magnetization directions, which allow additional optimization options when trying to create both loop and arc systems that fit geometric constraints. However, there are additional considerations that must be taken into account when transitioning these designs into a physical device.

For example, with larger volume ratios, there is a potential for the volume occupied by the magnets to overlap, as the two are too close to accommodate the larger volumes. This can be particularly problematic when attempting to create larger-order harmonics, as these naturally require more energy and therefore more magnetic material to produce. This is something that can be accounted for by setting a minimum separation between each χ_c value, such as setting $\chi_c^{n+1} - \chi_c^n > \delta$ where δ is a suitable distance that takes into account the thickness of the nth and $(n+1)$th magnets and manufacturing tolerances. This form of variable constraint is readily incorporated into a number of optimization algorithms. Similarly, constraints on the overall volume of each magnet may be useful to apply for accuracy purposes.

As the formulation does not incorporate a set magnetic volume, moving to excessively large magnet volumes may lead to error, particularly in small system sizes. Thus, care must also be taken around the size of the volume elements. As the overall cross-sectional area of the elements increases, they move further away from the infinitely thin elements modeled, and deviations from the derived model may become more noticeable. All structures considered here have cross-sectional areas less than the distance between magnets. For structures with significantly larger cross-sectional area, a secondary optimization to refine the spacings may yield greater field uniformity.

A further significant consideration is that, in general, the nested arrangements produce a lower field magnitude than the simple, single-set, arrangements. For example, the nested $\mathbf{B}_{1,0}$ set of Fig. 11 produces a field at the center, B_0, 1.31 times weaker than the corresponding single-magnet set. This issue is further illustrated by the $\mathbf{B}_{1,0}$ set, described in Fig. 5, which produces a field 8.70 times smaller. This is primarily a result of the opposing magnetization directions incorporated into both designs, which act to reduce the overall field magnitiude of the design. Thus, if overall field magnitude is a consideration, then care should be taken to find designs that limit the number of opposing magnets. Another possible solution can be seen in both the arc magnet cases, described in Sec. IV. Here, both the $\mathbf{B}_{1,1}$ (Fig. 7) and $\mathbf{B}_{2,1}$ (Fig. 9) arrangements produce higher field magnitudes than the single pairs, at 1.05 and 3.13 times stronger, respectively. This is achieved by the closer proximity of the magnets to the central region, which is only possible while maintaining field uniformity using the optimization procedure. As a result, the field magnitude can often be maintained and the

TABLE I. Table detailing the ratios of field magnitude, B_0, and field per unit magnet volume B_0/V for the structures detailed in Sec. III. All ratios are calculated with the single-magnet structure values as the numerator.

$B_{n,m}$	χ_c	B_0 ratio	B_0/V ratio
$\mathbf{B}_{1,0}$	0.3615 [0.2481, 0.3995, 0.4999]	8.70	13.8
$\mathbf{B}_{1,0}$	1.6939 [0.9221, 1.0701, 1.5243]	1.31	3.9
$\mathbf{B}_{1,1}$	2.5687 [1.1758, 1.2879, 1.8399]	0.95	6.45
$\mathbf{B}_{2,1}$	3.1290 [1.5381, 1.6335, 2.0888]	0.32	1.95

fidelity can be increased using a smaller overall system size. However, it should be noted that in both of these cases, while the field magnitude, B_0, of the system is larger, the field per unit material volume of the magnetic system is smaller. This is shown in further detail in Table I, with ratios of both B_0 and B_0/V between each set of simple and nested arrangements calculated.

This relationship between the nested arrangements and reduced field magnitude can be further mitigated by carefully choosing the number of error harmonics to null. While in each case above, we have chosen to target three error harmonics to reduce, this may not strictly be required to meet a given set of field tolerances. Thus, reducing the error harmonics nulled to two may increase the field magnitude, as the higher-order field harmonics require more energy to remove. Similarly, moving to two error harmonics would also incorporate more flexibility into the optimization algorithm, making finding solutions, which favor field magnitude easier to determine.

While weight has not been included in these considerations due to differences in density between common permanent magnet materials, it would similarly increase with the additional volume required in the nested designs. In general, we find that increasing the resulting magnetic field fidelity with this method comes with the detriment of increased magnet volume and weight. However, as mentioned, this can often lead to a smaller overall magnet geometry, suggesting careful management between magnetic field performance and SWaP parameters (namely, size and weight) is required for each system application.

Regarding manufacturability, as the optimization algorithm utilizes specific volume ratios between each set of primitives, it is possible to create the full design from the smallest volume element. The larger volume ratio elements simply comprise multiples of the smallest volume element. This procedure can be expanded, with the primitive structures themselves being broken down into multiple segments that can then be assembled into the prerequisite loop or arc. Although care must be taken not to remove too much material in this process, which may affect both field fidelity and magnitude, this can aid with meeting manufacturing limits such as minimum order requirements. Additionally, this can assist with assembly and reduce the risk of component damage due to the brittle nature of permanent magnets by reducing the size of finer volume elements.

VI. CONCLUSION

In this paper, we have presented a method of relating the magnetic field produced by sets of arcs or loops to the spherical harmonic content at their center for two magnetization directions: radial and axial. By incorporating the required magnetization direction into the permanent magnet Green's function and solving the resulting integral for the required geometry, we arrive at analytical expressions governing the expansion coefficients for each field harmonic produced. This reveals that both the axially and radially magnetized cases produce purely zonal harmonics in the loop geometry and purely tesseral harmonics in the arc geometry. The expansion coefficient expressions then form the basis of an optimization procedure, which is executed in *Mathematica*, allowing the optimal normalized separation, χ_c, for a set of multiple magnets with volume ratios V_i to be determined. This is accomplished by searching the user-defined parameter space for solutions to the underdetermined problem, which seeks to minimize the contribution of a number of error harmonics while maximizing the contribution from the target harmonic. The algorithm is then used to determine optimal, nested magnet sets. This is done for the zonal harmonic, $\mathbf{B}_{1,0}$, for the axially magnetized loops case and the tesseral harmonics, $\mathbf{B}_{1,1}$ and $\mathbf{B}_{2,1}$, for the radially magnetized arcs case. The resulting arrangements are computationally modeled using the ac/dc toolbox in COMSOL, alongside simple sets, with the resulting magnetic fields compared in each case. These nested magnet arrays produce substantially larger areas of uniformity than the simple, single-magnet set, results for each harmonic.

The optimization algorithm described in Sec. III C favored field uniformity in the construction of its cost function. However, this could be varied to incorporate the expansion coefficient expressions into a new procedure, which favored other constraints. As identified in Sec. V, sufficient field magnitude may be a challenge for some of the designs generated. Reconfiguring the optimization to target maximizing resulting field magnitude may aid for systems where this is a concern. This could also be accomplished by incorporating additional parameters such as the volume ratios within the optimization, rather than allowing them to be user-defined, allowing the field per magnetic material volume to be maximized. Furthermore, additional flexibility could be built into the optimization algorithm by allowing both ρ_c and d_c to vary independently, as opposed to the case of fixed ρ_c detailed in the

examples presented here. These modifications could be achieved in a number of well-documented optimization procedures, such as through Tikhonov regularization [45], or linear programming [46].

Although we have only shown one harmonic above first order, $\mathbf{B}_{2,1}$, the optimization procedure discussed is capable of generating harmonics above second order for both magnetization directions and geometries. The expressions for the respective expansion coefficients, $f_{n,m}$, of each of these options are not limited to low orders or degrees. While creating higher-order harmonics becomes progressively more difficult, as each requires more magnets to produce, this does conceivably allow the generation of complex physical magnetic fields. This requires that the fields can be well described with suitably feasible low-order harmonics and that the required expansion coefficients can be characterized and translated into corresponding strengths from each set of magnets (by varying remanent magnetization and volume).

The design procedure discussed could be further generalized to alternative magnetization directions and geometries. A variation of magnetization vector away from either purely $\hat{z}$ or $\hat{\rho}$ could be incorporated into the analytical expressions and then a similar procedure followed. Halbach arrays are one such magnetization arrangement that could be analyzed in such a fashion, with their magnetization vector mathematically well described. Similarly, other geometric arrangements could be incorporated; previous work on current-carrying wires has looked at ellipses, for example [16]. Passive shielding elements could also be incorporated, as accomplished for coil primitives in [47], though care must be taken in this instance to avoid any magnetization of the shielding environment, which would hamper its effectiveness.

ACKNOWLEDGMENTS

The authors acknowledge funding from UK Research and Innovation via QuSIT, the Quantum Sensing, Imaging and Timing hub program [EP/Z533166/1]. C. M., N. H., and M. F. are members of a University of Nottingham spinout, Contour Advanced Magnetic Design Ltd., which utilizes some of the methods described above.

DATA AVAILABILITY

There are no publicly available research data or software supporting this manuscript. Requests for further information or data should be sent to the authors.

APPENDIX A: MAGNETIC VS CURRENT COEFFICIENTS

As discussed in Sec. III A, the normalized spacings, χ_c, derived to remove the lead-error harmonic from a $\mathbf{B}_{1,0}$ field generated by a set of radially magnetized loops, are vastly different from those required to create a uniform field from a set of seemingly similar Helmholtz coils. This suggests that the harmonic content of loops of axially magnetized permanent magnets is fundamentally different to the harmonic content of loops of current-carrying wire, as it is clear that otherwise the two results would be identical. This can also be seen by comparing Eq. (22) to its previously derived counterpart for antisymmetric loops of wire (with current I) from [16],

$$f_{2v,0} = \frac{\pi I}{(2v)!}\frac{\partial^{2v}}{\partial \chi_c^{2v}}\left(\frac{\chi_c}{\sqrt{1+\chi_c^2}}\right). \tag{A1}$$

This serves to illustrate the clear functional differences between the two systems.

To further enable this discussion, here we derive the harmonic magnitudes, $f_{n,m}$, for a single loop of axially magnetized magnetic material centered at the origin. This can be accomplished by replacing Eq. (21) with,

$$M_{\text{loop}}(\mathbf{r}') = M_0\delta(\rho' - \rho_c)\delta(z'), \tag{A2}$$

and integrating as before. This only has solutions when $m = 0$ given by,

$$f^z_{n,0}(d_c = 0) = -\frac{1}{2\eta_{n,m}}\frac{(n+1)!}{n!}\frac{P_{n+1,0}(0)}{\rho_c^{n+1}}, \tag{A3}$$

which can be further simplified by evaluating $P_{n+1,0}(0)$ resulting in

$$f^z_{n,0}(d_c = 0) = \frac{(-1)^{(n-1)/2}}{2\eta_{n,0}}\frac{1}{\rho_c^{n+1}}\frac{(n+1)n!!}{(n+1)!!}, \tag{A4}$$

for odd n and 0 for even n. This is the opposite to what would typically be expected due to evaluating the $n+1$th value of $P_{n,m}$ rather than nth.

APPENDIX B: ADDITIONAL DESIGNS

As mentioned in Sec. IV, the simple analytical solution to generate $\mathbf{B}_{1,0}$ for the loops case has two results. Here we discuss the nested variant of the larger spaced $\chi_c = 1.6939$ design to further detail the methods capabilities and offer comparisons between tightly constrained or more open χ_c parameter spaces. To accommodate the larger system size, the optimization was performed within the limits of $\chi_{\text{min}} = 0.7$ and $\chi_{\text{max}} = 1.7$. In this case, volume ratios of $V_i = [1, -2, 4]$ were determined via user input, with $\chi_c = [0.9221, 1.0701, 1.5243]$ returned from the optimization algorithm. The resulting magnet arrangement is illustrated in Fig. 11(b), along with the simpler design attainable from analytics alone in Fig. 11(a).

As with the smaller solution to generating a $\mathbf{B}_{1,0}$ harmonic, the single pair and nested designs were simulated for a fixed ρ_c and are compared in Fig. 12. Assuming

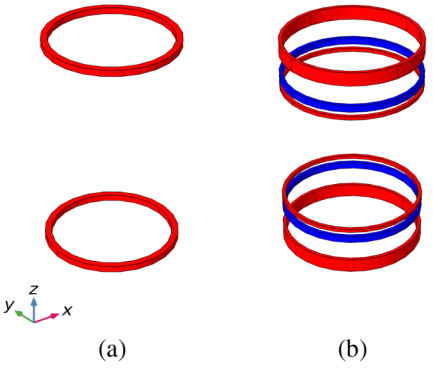


FIG. 11. Schematic illustration of (a) a simple loop pair with $\chi_c = 1.6939$ and (b) a nested loop set with $\chi_c = [0.9221, 1.0701, 1.5243]$ and volume ratios of $V_i = [1, -2, 4]$, respectively. All loops have radius ρ_c and designed to generate $\mathbf{B}_{1,0}$. Magnetization along positive (negative) $\hat{z}$ is shown in red (blue). The axis is common across both diagrams.

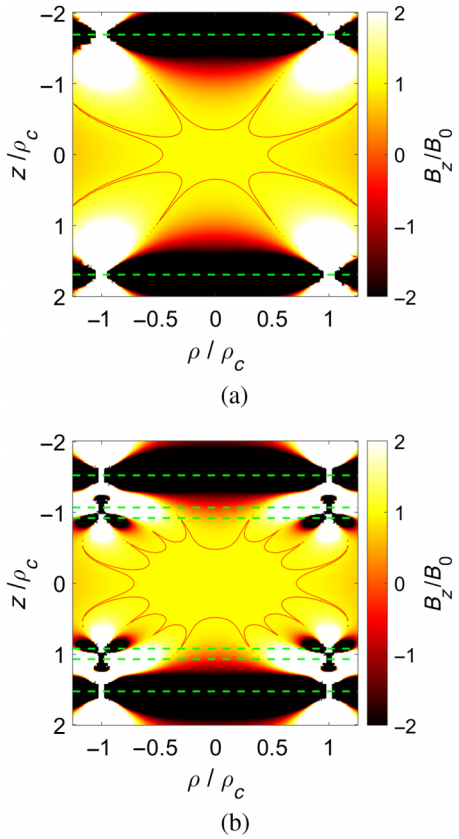


FIG. 12. Normalized axial ($\hat{z}$) field, $\bar{B} = B_z/B_0$ (where $B_0 = B_z(z = 0, \rho = 0)$), plotted in the xz plane for (a) single loop magnet set with $\chi_c = 1.6939$ is shown in Figs. 11(a) and 11(b) nested loop set with $\chi_c = [0.9221, 1.0701, 1.5243]$ and volume ratios $V_i = [1, -2, 4]$ is shown in Fig. 11(b). All magnets are magnetized in the $\hat{z}$ direction, ρ_c is kept constant across all figures, and all configurations are optimized to generate the $\boldsymbol{B_{1,0}}$ harmonic. Solid red contours enclose the area where the uniform B_z fields deviate from uniformity by 1%, and green dashed lines indicate positions of magnets in the xz plane.

a larger axial range target region with z between $-2\rho_c$ and $2\rho_c$ to encompass the full geometry of the magnets, this comparison illustrates a comparative increase in the region where the field deviates by less than 1% of a factor of 1.7235 for the nested design of Fig. 12(b).

The resulting ratios of magnetic field strength (B_0) and field per unit volume ratios (B_0/V) are also illustrated in Table I. They show that this design, while featuring only a moderate increase in uniform region volume, generates significantly more field and requires less volume than the other $\mathbf{B}_{1,0}$ nested design (with parameters $\chi_c = [0.2481, 0.3995, 0.4999]$ and $V_i = [-1, 2, -2]$). We attribute this to the more flexible constraints on χ_c compared with the other design ($\chi_{\max} = 1.7$ vs $\chi_{\max} = 0.5$). This results in a more flexible optimization, allowing the design to find a result for which less volume of material is magnetized in opposing directions. It should be noted that, as expected, both nested loop designs for $\mathbf{B}_{1,0}$ generate less magnetic field per unit volume than the simple, single pair analytical results.

[1] J. Reichel, W. Hänsel, and T. W. Hänsch, Atomic micromanipulation with magnetic surface traps, Phys. Rev. Lett. **83**, 3398 (1999).

[2] H. J. Metcalf and P. Van der Straten, *Laser Cooling and Trapping* (Springer Science & Business Media, New York, 1999).

[3] S. Gov, S. Shtrikman, and H. Thomas, Magnetic trapping of neutral particles: Classical and quantum-mechanical study of a Ioffe–Pritchard type trap, J. Appl. Phys. **87**, 3989 (2000).

[4] T. Schönau, T. Scholtes, F. Wittkämper, A. Sekels, S. Hiebel, G. Oelsner, and R. Stolz, Optically pumped vector magnetometer using a strong bias magnetic field, Phys. Rev. Appl. **23**, 024006 (2025).

[5] Z.-X. Meng, P.-Q. Yan, S.-Z. Wang, X.-J. Li, H.-B. Xue, and Y.-Y. Feng, Closed-loop dual-atom-interferometer inertial sensor with continuous cold atomic beams, Phys. Rev. Appl. **21**, 034050 (2024).

[6] J. Wang, L. Zhou, R.-B. Li, M. Liu, and M.-S. Zhan, Cold atom interferometers and their applications in precision measurements, Front. Phys. China **4**, 179 (2009).

[7] R. Geiger, A. Landragin, S. Merlet, and F. Pereira Dos Santos, High-accuracy inertial measurements with cold-atom sensors, AVS Quantum Sci. **2**, 024702 (2020).

[8] B. Wu, Z. Wang, B. Cheng, Q. Wang, A. Xu, and Q. Lin, The investigation of a μgal-level cold atom gravimeter for field applications, Metrologia **51**, 452 (2014).

[9] A. Borna, J. Iivanainen, T. R. Carter, J. McKay, S. Taulu, J. Stephen, and P. D. D. Schwindt, Cross-axis projection error in optically pumped magnetometers and its implication for magnetoencephalography systems, NeuroImage **247**, 118818 (2022).

[10] R. Dawson, M. S. Mrozowski, D. Hunter, C. O'Dwyer, E. Riis, P. Griffin, S. Ingleby *et al.*, A triaxial vectorization technique for a single-beam zero-field atomic magnetometer to suppress cross-axis projection error, arXiv:2408.12994.

[11] R. Turner, A target field approach to optimal coil design, J. Phys. D **19**, L147 (1986).
[12] F. Roméo and D. I. Hoult, Magnet field profiling: Analysis and correcting coil design, Magn. Reson. Med. **1**, 44 (1984).
[13] M. Packer, P. J. Hobson, N. Holmes, J. Leggett, P. Glover, M. J. Brookes, R. Bowtell, and T. M. Fromhold, Optimal inverse design of magnetic field profiles in a magnetically shielded cylinder, Phys. Rev. Appl. **14**, 054004 (2020).
[14] M. Packer, P. J. Hobson, N. Holmes, J. Leggett, P. Glover, M. J. Brookes, R. Bowtell, and T. M. Fromhold, Planar coil optimization in a magnetically shielded cylinder, Phys. Rev. Appl. **15**, 064006 (2021).
[15] R. Zetter, A. J. Mäkinen, J. Iivanainen, K. C. J. Zevenhoven, R. J. Ilmoniemi, and L. Parkkonen, Magnetic field modeling with surface currents. Part II. Implementation and usage of bfieldtools, J. Appl. Phys. **128** 063905 (2020).
[16] P. J. Hobson, N. L. Hardwicke, A. Davis, T. Smith, C. Morley, M. Packer, N. Holmes, M. A. Weil, M. Brookes, R. Bowtell, and M. Fromhold, Designing optimal loop, saddle, and ellipse-based magnetic coils by spherical harmonic mapping, arXiv:2305.00572.
[17] I. R. Hill, Y. B. Ovchinnikov, E. M. Bridge, E. A. Curtis, and P. Gill, Zeeman slowers for strontium based on permanent magnets, J. Phys. B **47**, 075006 (2014).
[18] A. Parsagian and M. Kleinert, Designing and building a permanent magnet Zeeman slower for calcium atoms using a 3D printer, Am. J. Phys. **83**, 892 (2015).
[19] J. M. D. Coey, Permanent magnet applications, J. Magn. Magn. Mater. **248**, 441 (2002).
[20] F. Florio, G. Sinha, and R. Sundararaman, Designing high-accuracy permanent magnets for low-power magnetic resonance imaging, IEEE Trans. Magn. **54**, 1 (2018).
[21] C. Hugon, F. D'Amico, G. Aubert, and D. Sakellariou, Design of arbitrarily homogeneous permanent magnet systems for NMR and MRI: Theory and experimental developments of a simple portable magnet, J. Magn. Reson. **205**, 75 (2010).
[22] G. Moresi and R. Magin, Miniature permanent magnet for table-top NMR, Concepts Magn. Reson., Part B **19**, 35 (2003).
[23] S. C. Scholten, A. J. Healey, I. O. Robertson, G. J. Abrahams, D. A. Broadway, and J.-P. Tetienne, Widefield quantum microscopy with nitrogen-vacancy centers in diamond: Strengths, limitations, and prospects, J. Appl. Phys. **130**, 150902 (2021).
[24] S.-Y. Hou, G. Feng, Z. Wu, H. Zou, W. Shi, J. Zeng, C. Cao, S. Yu, Z. Sheng, X. Rao *et al.*, SpinQ Gemini: A desktop quantum computing platform for education and research, Eur. Phys. J. Quantum Technol. **8**, 1 (2021).
[25] I. Pogorelov, T. Feldker, C. D. Marciniak, L. Postler, G. Jacob, O. Krieglsteiner, V. Podlesnic, M. Meth, V. Negnevitsky, M. Stadler *et al.*, Compact ion-trap quantum computing demonstrator, PRX Quantum **2**, 020343 (2021).
[26] H. Aman and T. Plakhotnik, Accuracy in the measurement of magnetic fields using nitrogen-vacancy centers in nanodiamonds, J. Opt. Soc. Am. B **33**, B19 (2016).
[27] N. P. de Leon, K. M. Itoh, D. Kim, K. K. Mehta, T. E. Northup, H. Paik, B. S. Palmer, N. Samarth, S. Sangtawesin, and D. W. Steuerman, Materials challenges and opportunities for quantum computing hardware, Science **372**, eabb2823 (2021).
[28] T. Strohm, K. Wintersperger, F. Dommert, D. Basilewitsch, G. Reuber, A. Hoursanov, T. Ehmer, D. Vodola, and S. Luber, Ion-based quantum computing hardware: Performance and end-user perspective, arXiv:2405.11450.
[29] S. Noguchi, S. B. Kim, S. Hahn, and Y. Iwasa, Passive shimming by eliminating spherical harmonics coefficients of all magnetic field components generated by correction iron pieces, IEEE Trans. Magn. **50**, 605 (2014).
[30] F. X. Li, J. P. Voccio, M. C. Ahn, S. Hahn, J. Bascuñán, and Y. Iwasa, An analytical approach towards passive ferromagnetic shimming design for a high-resolution nmr magnet, Supercond. Sci. Technol. **28**, 075006 (2015).
[31] X. Zhu, H. Wang, H. Wang, Y. Li, and Y. Fang, A novel design method of passive shimming for 0.7-T biplanar superconducting mri magnet, IEEE Trans. Appl. Supercond. **26**, 1 (2016).
[32] S. Noguchi, S. Kim, S. Hahn, and Y. Iwasa, Passive shimming by eliminating spherical harmonics coefficients of all magnetic field components generated by correction iron pieces, IEEE Trans. Magn. **50**, 605 (2014).
[33] R. Schmied, D. Leibfried, R. J. C. Spreeuw, and S. Whitlock, Optimized magnetic lattices for ultracold atomic ensembles, New J. Phys. **12**, 103029 (2010).
[34] Z. Y. Lu, G. S. Xu, D. H. Chen, L. Chen, X. Y. Zhang, M. Y. Ye, and B. N. Wan, Design of quasi-axisymmetric stellarators with variable-thickness perpendicular permanent magnets based on a two-step magnet design strategy, Nucl. Fusion **61**, 106028 (2021).
[35] G. S. Xu, Z. Y. Lu, D. H. Chen, L. Chen, X. Y. Zhang, X. Q. Wu, M. Y. Ye, and B. N. Wan, Design of quasi-axisymmetric stellarators with varying-thickness permanent magnets based on fourier and surface magnetic charges method, Nucl. Fusion **61**, 026025 (2021).
[36] P. J. Hobson, C. Morley, A. Davis, T. Smith, and M. Fromhold, Target-field design of surface permanent magnets, Phys. Rev. Appl. **22**, 034015 (2024).
[37] W. Zhou, B. Han, J. Wang, D. Wu, F. Zhao, and N. Li, Design of uniform magnetic field coil by quasi-elliptic function fitting method with multiple optimizations in miniature atomic sensors, IEEE Trans. Ind. Electron. **69**, 11755 (2022).
[38] J. L. Kirschvink, Uniform magnetic fields and double-wrapped coil systems: Improved techniques for the design of bioelectromagnetic experiments, Bioelectromagnetics **13**, 401 (1992).
[39] H. Sanchez Lopez, Feng Liu, E. Weber, and S. Crozier, Passive shim design and a shimming approach for biplanar permanent magnetic resonance imaging magnets, IEEE Trans. Magn. **44**, 394 (2008).
[40] J. Lee and J. Yoo, Topology optimization of the permanent magnet type MRI considering the magnetic field homogeneity, J. Magn. Magn. Mater. **322**, 1651 (2010).

[41] K. Halbach, Design of permanent multipole magnets with oriented rare earth cobalt material, Nucl. Instrum. Methods **169**, 1 (1980).

[42] S. Tewari, T. O'Reilly, and A. Webb, Improving the field homogeneity of fixed-and variable-diameter discrete Halbach magnet arrays for MRI via optimization of the angular magnetization distribution, J. Magn. Reson. **324**, 106923 (2021).

[43] I. Rehberg and P. Blümler, Analytic approach to creating homogeneous fields with finite-size magnets, Phys. Rev. Appl. **23**, 064029 (2025).

[44] J. D. Jackson, *Classical Electrodynamics*, 1st ed. (Wiley, New York, NY, 1962), pp. 156–158.

[45] J. M. Jackson, M. A. Brideson, L. K. Forbes, and S. Crozier, Tikhonov regularization approach for acoustic noise reduction in an asymmetric, self-shielded mri gradient coil, Concepts Magn. Reson., Part B **37**, 167 (2010).

[46] H. Xu, S. M. Conolly, G. C. Scott, and A. Macovski, Homogeneous magnet design using linear programming, IEEE Trans. Magn. **36**, 476 (2000).

[47] M. Packer, P. J. Hobson, A. Davis, N. Holmes, J. Leggett, P. Glover, N. L. Hardwicke, M. J. Brookes, R. Bowtell, and T. M. Fromhold, Magnetic field design in a cylindrical high-permeability shield: The combination of simple building blocks and a genetic algorithm, J. Appl. Phys. **131**, 093902 (2022).